UCRL-JC--106127
DE91 008505

Nondestructive Imaging of Materials Microstructure Using X-ray Tomographic Microscopy

J. H. Kinney
M. C. Nichols
U. Bonse
S. R. Stock
T. M. Breunig
A. Guvenilir
R. A. Saroyan

Materials Research Society
Fall Meeting
Boston, MA
November 27, 1990

November 1990

Lawrence Livermore National Laboratory

unclassified

NONDESTRUCTIVE IMAGING OF MATERIALS MICROSTRUCTURES USING X-RAY TOMOGRAPHIC MICROSCOPY

J.H. KINNEY*, M.C. NICHOLS**, U.BONSE†,S.R. STOCK††, T.M. BREUNIG††, A. GUVENILIR†† AND R.A. SAROYAN*

*Chemistry and Materials Sciences Department, Lawrence Livermore National Laboratory, Livermore CA 94550
**Sandia National Laboratories, Livermore CA 94550
†Department of Physics, University of Dortmund, Dortmund Germany
††School of Materials Engineering, Georgia Institute of Technology, Atlanta GA 30332

ABSTRACT

A technique for nondestructively imaging microstructures of materials *in situ*, especially a technique capable of delineating the time evolution of chemical changes or damage, will greatly benefit studies of materials processing and failure. X-ray tomographic microscopy (XTM) is a high resolution, three-dimensional inspection method which is capable of imaging composite materials microstructures with a resolution of a few micrometers. Because XTM is nondestructive, it will be possible to examine materials under load or during processing, and obtain three-dimensional images of fiber positions, microcracks, and pores. This will allow direct imaging of microstructural evolution, and will provide time-dependent data for comparison to fracture mechanics and processing models.

INTRODUCTION

The spatial resolution of x-ray CT has been improved by several orders of magnitude during the past decade. It is now possible, using x-ray CT, to three-dimensionally image materials microstructures with a resolution of a few micrometers in millimeter-size samples. Efforts are underway to improve this resolution and, at the same time, to increase the sample dimensions which can be imaged with this technique. Nevertheless, the resolution and sensitivity of x-ray CT are sufficient to make significant inroads into our understanding of how mechanical properties are affected by changes in microstructure. The impact of x-ray CT methods will be especially felt in the study of processing and failure in advanced composite materials. Noninvasive, *in-situ* CT observations of advanced composites will provide time-resolved information regarding the evolution of microstructure—information which currently is only indirectly inferred from *post-mortem* examinations and large statistical sampling of as-prepared material.

This paper provides details about a CT technique we have been developing these past several years. We call this technique x-ray tomographic microscopy (XTM) to distinguish it as a form of x-ray microscopy which utilizes tomographic reconstruction techniques to form three-dimensional images. The paper is presented in three parts. The first part discusses critical issues involved in performing XTM, such as the optimization of the detector and the x-ray energy. The second part discusses

three examples of the application of XTM to imaging fiber composite microstructures. These examples represent progressively more complicated fiber geometries beginning with uniaxially aligned fibers and concluding with woven (balanced plain weave) fibers. The third part discusses our present efforts to perform *in–situ* materials studies, and outlines future directions of research. Throughout this paper, the emphasis is placed on imaging advanced composites which have technological importance. XTM is a powerful technique, however, and its application to other areas such as electronic materials, biomaterials, and geology can be anticipated.

X–RAY TOMOGRAPHIC MICROSCOPY

X–ray tomographic microscopy (XTM) using synchrotron radiation has been shown to be an effective, high–resolution, three dimensional imaging technique for nondestructive characterization of materials [1,2]. XTM differs from conventional optical and electron–beam microscopy in that the sample need not be harmed prior to characterization of internal microstructure. There is no requirement for flat optical surfaces or thin sections; materials are examined in their unaltered state. XTM measures the x–ray attenuation coefficient, μ, at a point $r_{x,y,z}$ in a material from a finite set of x–ray attenuation measurements (projection data) taken at different angles through the sample. The projection data is the transmitted x–ray intensity reaching a position sensitive detector after passing through the sample. The absorption data is directly related to the materials microstructure, and is given, for a single point on the detector, by

$$I=\int S(E)[\exp-\int\mu(x,y,z,E)dl\ ]\ dE, \qquad (1)$$

where S(E) is the energy spectrum of the x–ray source and $\mu(x,y,z,E)$ is the energy dependent attenuation coefficient at a single point along the projection. The integral is taken along a straight path dl through the sample. If the x–rays are made nearly monochromatic with photon energy E_O, the energy spectrum can be approximated by a delta function and Equation 1 reduces to the familiar form of the Radon transform [3]:

$$\ln\left(\frac{I_O}{I}\right) = \int\mu(x,y,z,E_O)dl\ . \qquad (2)$$

Measurements of the attenuation through the sample as a function of angle and position are used to numerically invert Equation 2 to solve for $\mu(x,y,z,E_O)$. The number of angular views considered sufficient for this inversion (reconstruction) is approximated using simple geometric arguments by

$$R\Delta\Theta = W \qquad (3)$$

where R is the maximum outward extent of the sample from the center of rotation, $\Delta\Theta$ is the suggested angular increment and W is the projection width. A typical value for R with the present XTM is 2 mm and W is 5 μm. The angular increment sufficient for the reconstruction using these dimensions is approximately 0.2 degrees, although increments of 0.5 degrees are generally used in practice.

Conventional CT measurements involve collecting absorption information for a single cross-sectional slice through a material. Spatial resolution is achieved either by collimating the incident beam using a pinhole, and then rastering the beam across the sample for every angular setting, or by using a position sensitive detector to measure all of the projection data for a single angular view in parallel. Aside from its relative simplicity, the advantage of the pinhole technique is that the resolution, to first order, is determined only by the size of the collimator. Elliott and Dover have successfully used pinhole scanning with a standard x-ray generator to perform tomography on mineralized tissues [4] and composites [5]. An energy dispersive detector is used to count photons of only a single energy, thereby satisfying the requirement for nearly monochromatic radiation.

The primary disadvantage using the pinhole is that most of the incident radiation is thrown away. The rastering technique, therefore, is extremely time consuming. Acquiring the data for the reconstruction of a single cross section of a sample takes upwards of 12 or more hours depending on the size of the pinhole collimator and the sample. This limits the utilization of the pinhole approach for three-dimensional analysis and precludes real time studies.

Linear photodiode arrays have been used in a number of CT devices designed to operate on conventional x-ray sources [6,7]. The widespread application of linear photodiode arrays results from both their ease of use and ability to acquire upwards of a thousand projected rays simultaneously. The parallel acquisition of data improves the speed of the measurements nearly a thousandfold, and the accumulation of enough data to reconstruct a single slice becomes measured in minutes rather than days. In spite of these advantages, however, there are drawbacks to the use of the photodiode array for ultrahigh resolution characterization. The first of these drawbacks is that the photodiode array is noisy and is subject to nonlinearities. This noise limits the dynamic range and therefore the maximum contrast which can be studied in a sample. The nonlinearities introduce ring-like artifacts in the reconstructions which can further reduce the usefulness of the information obtained, although these effects can be partially reduced by using a combination translate-rotate design. Finally, even with reducing the data acquisition times for a single slice from days to hours, it still requires days to obtain enough information for three-dimensional sample visualization.

Clearly, a two-dimensional array which records projection data for many contiguous slices simultaneously is essential for practical three-dimensional imaging [8]. Feldkamp uses a vidicon array as a two-dimensional detector [9]. Because a vidicon is continuously read out at video rates, the integration times are too short to detect an x-ray image using a laboratory x-ray source. Therefore, Feldkamp relies on an image intensifier which converts the x-ray photons into visible photons and then amplifies the light signal by orders of magnitude. Because image intensifiers have relatively low spatial resolution, it is necessary to use a microfocus source in a magnifying geometry, and a "cone-beam" algorithm is necessary to reconstruct the three-dimensional image from the x-ray projection data[10]. CT systems run in this manner are limited in spatial resolution by the source spot size (~20-25 μm), and in sensitivity by the photon statistics and linearity of the image intensifier. Good photon statistics are difficult to

achieve because signal averaging with vidicons is limited by excessive read-out noise. Nevertheless, the image intensifier with vidicon detector has been adopted by others [11], and images of 20–30 μm resolution have been demonstrated when imaging high contrast features.

Our group has developed an XTM instrument which uses a thermoelectrically–cooled charge coupled device detector (CCD) in place of a vidicon array [12]. The CCD provides superior spatial resolution and noise properties, and can be integrated over time periods of several minutes with little buildup of dark current noise. Because of this, imaging can be performed without the complications and image degradation of an intensifier. Furthermore, the detecting system we have configured can be operated successfully using standard focus x–ray tubes as well as microfocus sources and synchrotron radiation. With the standard focus source, the sample is placed in close proximity to the scintillator to minimize the penumbral blurring due to the diverging beam. In this configuration, a parallel beam reconstruction algorithm is used. With a microfocus source, the sample can be placed much closer to the source in order to take advantage of an x–ray magnifying geometry using a cone–beam reconstruction algorithm. Since its development, XTM using CCD arrays has been successfully tested using synchrotron radiation at the Stanford Synchrotron Radiation Laboratory 13,14], at the DORIS storage ring at the Hamburg Synchrotron Radiation Laboratory [15], at the National Synchrotron Light Source [16], at the Cornell High Energy Synchrotron Source (CHESS), and most recently using laboratory x–ray sources.

The sample positioning hardware currently consists of translation stages, a rotary stage, and the stage controllers and driver electronics. The hardware now in use is from Klinger Scientific. All stages have stepper drive motors, incremental position encoders and an origin signal. The linear stages also have plus– and minus– limit signals. The stage controller provides both user and computer interfaces to up to eight separate stages. The user interface consists of front panel displays of position with a separate button for each axis. Also, there are front panel buttons which allow the user to independently position each axis or to home each axis to its origin position. The computer interface, as it is used here, is an IEEE–488 port, through which the controller can accept commands from a computer telling it how and where to position the eight axes and through which it can report back to the computer its success or failure at executing the commands.

In operation, the sample is removed from the beam with a linear translation stage. A reference image ($I_O(x,y)$ in Eq. 1) is recorded and the sample is moved back into the beam. A radiograph of the sample is taken ($I(x,y)$ in Eq. 1), and the image data are stored in the computer memory. This procedure is incrementally repeated until a full 180 degrees of sample rotation has been recorded. The reason for the reference images is to monitor the incident beam profile. For a very stable source, the frequency at which reference images are taken can be reduced.

A single crystal scintillator screen converts x-rays into visible light which is imaged with the CCD. Initially, the scintillator consisted of ball-milled sub-micron particles of phosphor. The phosphor layer was thin with respect to the optical path length, and suspended on a glass substrate with a transparent binder. Though great care was taken in fabricating the phosphor, the spatial resolution was no better than 20 μm because of optical

scatter caused by differences in the indices of refraction between the phosphor and the binder, and between the binder and the substrate.

In the present configuration, we use a single crystal $CdWO_4$ scintillator. $CdWO_4$ is not hygroscopic and has a very high x–ray stopping power. Optical scatter off of the free surface is minimized by using an anti–reflective coating. Measurements using synchrotron radiation sources at 20 keV indicate that the spatial resolution of the scintillator is better than 5 μm.

The resolution of a single crystal scintillator is not perfect, however. First, x–rays have a finite depth of penetration, and this depth increases with increasing energy. Second, secondary events such as fluorescence, photoelectron production and scatter act to blur the image within the scintillator. The first effect, a finite depth of penetration, reduces the image contrast. The secondary effects reduce the resolution. Unfortunately, both of these problems increase with increasing energy, and are related to each other by the modulation transfer function, MTF, of the system.

Figure 1 shows the depth of x–ray penetration in $CdWO_4$ as a function of incident x–ray energy. The depth has been calculated as the path length over which 90% of the scintillation events occur. As x–ray energy rises above 20 keV, the penetration becomes significant, and the loss of subtle contrast variations in a sample becomes unavoidable. Also plotted in Fig. 1 is the depth of x–ray penetration in CsI, a widely used scintillator material.

Two approaches have been developed to improve the resolution of scintillator screens. The first approach is to decrease the thickness of the scintillator. The second approach is to segment the scintillator into very small optically isolated pieces[17,18]. In this manner, light produced by x–ray absorption is confined to a single region of the scintillator. Making the scintillator thinner reduces the amount of contrast loss, but greatly decreases

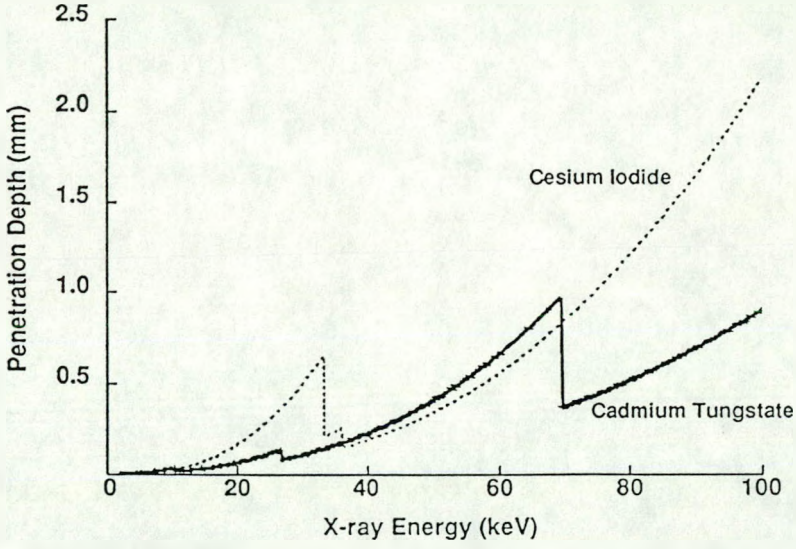

Figure 1: X–ray penetration depth (90% absorption) in single crystal scintillators.

the light output of the scintillator. Segmentation, on the other hand, offers the advantage that as the x–ray energy increases, the scintillator can be made thicker, thereby allowing more efficient use of the x–ray flux. The difficulty of segmentation lies in fabricating very small elements and in keeping them optically isolated. Exxon has had some success in growing 1μm columns of CsI crystals for a high resolution scintillator. Though the isolated columns are 1 μm and less in diameter and roughly 1 μm apart, a careful examination of Exxon's published radiographs indicates that the spatial resolution is not as high as the segmentation would lead us to believe. Though it is difficult to speculate on the cause for this poorer than expected performance, two possibilities are worth considering. The first possibility is that the scintillator face plate (the substrate upon which the CsI is grown) has a different index of refraction than the CsI, thereby leading to optical scatter. The second possibility is that the individual segments of the scintillator are not isolated from secondary x–ray effects.

X–ray scatter (defined here as including all secondary processes) may be the ultimate limiting factor in the resolution of scintillator screens. At the x–ray energies considered here (< 100 keV), an x–ray photon can either be absorbed or scattered. In high Z materials the incoherent scattering probability is small at these energies; hence, the predominant interaction is through absorption. When an x–ray photon is absorbed, the excited atom can decay by emitting fluorescent radiation. The fluorescent radiation is emitted into a 4π solid angle, and can travel for considerable distances before being absorbed. This fluorescent radiation creates additional scintillation events which can be far removed from the original photon path. Also, the absorption of x–rays leads to the production of energetic photoelectrons. The energy of the photoelectron is given by $E_e = h\nu - \phi_b$, where ϕ_b is the binding energy of the electron and $h\nu$ is the energy of the absorbed x–ray. The photoelectrons are sufficiently energetic to travel for considerable distances in the scintillator, creating scintillation events all along their path. Each of these events lead to a loss of spatial resolution and an increase in noise.

We have calculated the effects on resolution due to secondary events in $CdWO_4$ as a function of x-ray energy using the Monte Carlo code COG [19]. COG follows all primary and subsequent generations of photons until they are either absorbed or leave the scintillator. Photoelectric processes and incoherent and coherent scattering processes are considered in the calculations. The results of these calculations suggest that the largest contributor to secondary scintillation events is the emission of photoelectrons during the stopping of the x-rays.

The photoelectron range depends strongly on the incident x–ray energy. Photoelectrons have much greater penetration in CsI than in $CdWO_4$, principally because the electron binding energy increases with Z and the photoelectron range decreases with increasing density. The large range of the photoelectrons in CsI (>1 μm) makes it impossible to isolate scintillator segments on the micron scale. It is important to note, however, that the spatial resolution of the scintillator is optimal immediately above an absorption edge where the depth of x-ray penetration and photoelectron energy are at their lowest.

Though laboratory x–ray sources can be used for XTM, synchrotron radiation is the optimal source. Synchrotron radiation provides a broad

Though laboratory x–ray sources can be used for XTM, synchrotron radiation is the optimal source. Synchrotron radiation provides a broad banded source of x–rays which range in energy from a few eV to several tens of keV. Because synchrotron radiation can be continuously tuned using a single crystal monochromator, it is possible to select the optimum x–ray energy for the sample being characterized. Frequently, it is desired to choose an x–ray energy which optimizes the signal–to–noise for the sample. The optimum energy is given by the well known relationship

$$D = \frac{2}{\mu} \tag{4}$$

Figure 2 shows the optimum sample diameter, D, as a function of x–ray energy for three important classes of materials used in composite manufacture: aluminum, silicon carbide, and titanium aluminide. Also depicted in Fig. 2 are the energy intervals which can reasonably be spanned with present and proposed synchrotron radiation sources. Test panels of metal matrix composites are typically 1.5mm thick. Assuming that the aspect ratio of a rectangular gauge tensile specimen should be at least three to one, then the largest dimension through the gauge section will be about 5mm. In ceramic matrix composite (CMC) specimens, for example Nicalon fibers (Nicalon is an amorphous SiC fiber) in a SiC matrix, the panel thickness is typically 3mm, giving a largest dimension through the gauge of approximately 10mm.

Using Fig. 2, the optimal x–ray energy for imaging Al–matrix material will be 27 keV, for imaging SiC material will be 37 keV and for imaging higher Z intermetallics such as Ti_3Al will be 52 keV. Although the National Synchrotron Light Source (NSLS) does not provide adequate x–ray flux at

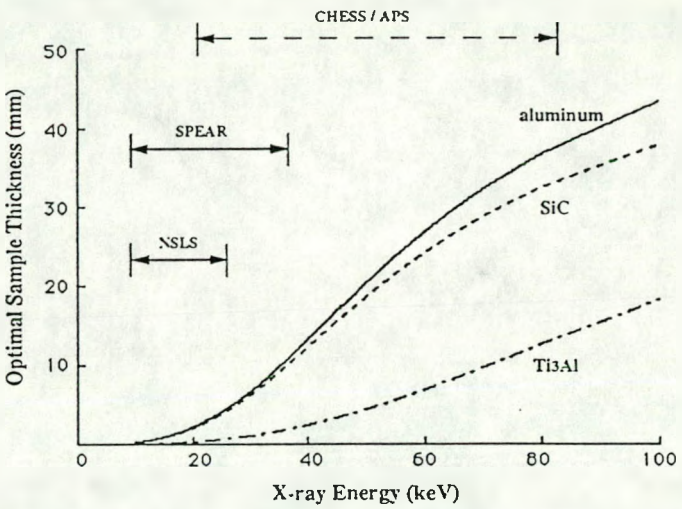

Figure 2: The optimal x–ray energy for imaging typical composite materials as a fuction of thickness.

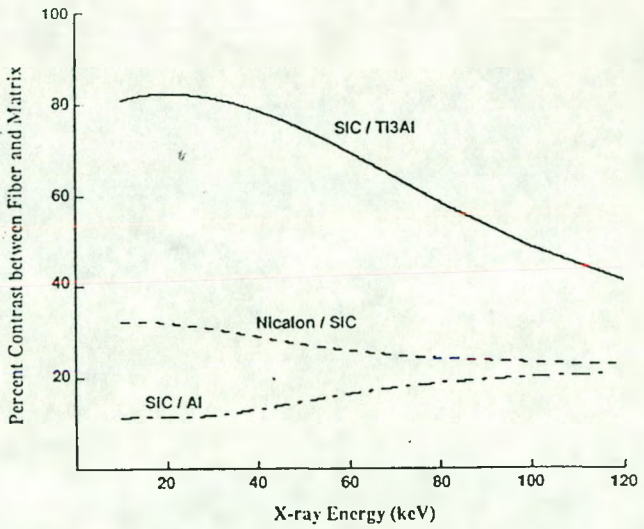

Figure 3: X–ray contrasts ($100x|\mu_f-\mu_m|/\mu_m$) between fiber and matrix for three typical composite systems.

the high energies required for penetrating composites with these gauge sections, the hard x–ray wiggler beamline on the SPEAR storage ring at Stanford is well suited for imaging the CMCs as well as the aluminum–based composites. For the more absorbing intermetallic composites, it will be necessary to use the wiggler beamlines at Cornell which can provide the required flux at high energies. The proposed Advanced Photon Source (APS) will also be well suited to imaging materials microstructures of the intermetallic composites.

In an x–ray image, contrast between features arises from differences in the x–ray attenuation coefficient. High contrast features occur when cracks and high Z or high density inclusions are present in the sample. Weak contrasts result from slight variations in material composition. Figure 3 represents the contrast between matrix and fiber as a function of x–ray energy for three cases: 1) SiC–fiber (SCS8) in an Al matrix, 2) Nicalon fiber in a SiC matrix, and 3) SiC–fiber (SCS6) in a titanium–aluminide matrix. The contrast between SiC and Al is only 10% over a broad energy range. Therefore, distinguishing the fiber from the matrix in this composite system requires excellent photon statistics. The higher contrast between SiC and CAS, on the other hand, relaxes the statistical constraints somewhat. The contrast is highest between the SiC and the intermetallic Ti_3Al. At low x–ray energy, the contrast is as high as 80%. Thus, in this composite system, the fibers are clearly identified in the presence of noise. However, the high contrast poses another problem; namely, it becomes difficult to distinguish broken fibers from voids and pores!

EXAMPLES

We consider three examples of the application of XTM to imaging composite microstructures. These examples have been chosen to represent progressively more complicated fiber geometries. All of the data were

acquired during a run at the Cornell High Energy Synchrotron Source (CHESS) using the 6–pole wiggler end station on beamline A2. Silicon monochromator crystals were used, with (111),(311), and (400) reflections chosen to cover the x–ray energy range from 20 to 60 keV used in the experiments.

The first example is that of an aluminum matrix—SCS8 silicon carbide fiber composite. SCS8 fibers consist of a 32–μm diameter carbon core surrounded by an approximately 140–μm diameter SiC sheath. An approximately 1–μm thick carbon coating is deposited onto the fiber to protect it from detrimental chemical reactions with the matrix phase during consolidation. The composite is approximately 1.5 mm thick and consists of 8 plies of uniaxially aligned fibers. The composite has failed in tension, and XTM was performed from the fracture surface down about 2 mm along the long axis of the composite. The pixel sampling size was 5.6 μm, and 0.5 degree angular increments were used. The x–ray energy was 20 keV.

Figure 4 shows an XTM slice taken in the vicinity of the fracture surface. It is important to emphasize that the cross section is taken through bulk material, and that no surface preparation was necessary. Hence, none of the artifacts frequently associated with polishing, such as fiber pull–out, need to be considered when interpreting the XTM image. The image in Fig. 4, therefore, is of the undisturbed region beneath and bordering the fracture surface. In Fig. 4 it is observed that the fibers have apparently failed at the graphite core–SiC interface in the fiber interiors, and not at the fiber–matrix interphase as we had expected. The impact of these observations on our understanding of mechanical failure in this composite system is presented in more detail later in these proceedings[20].

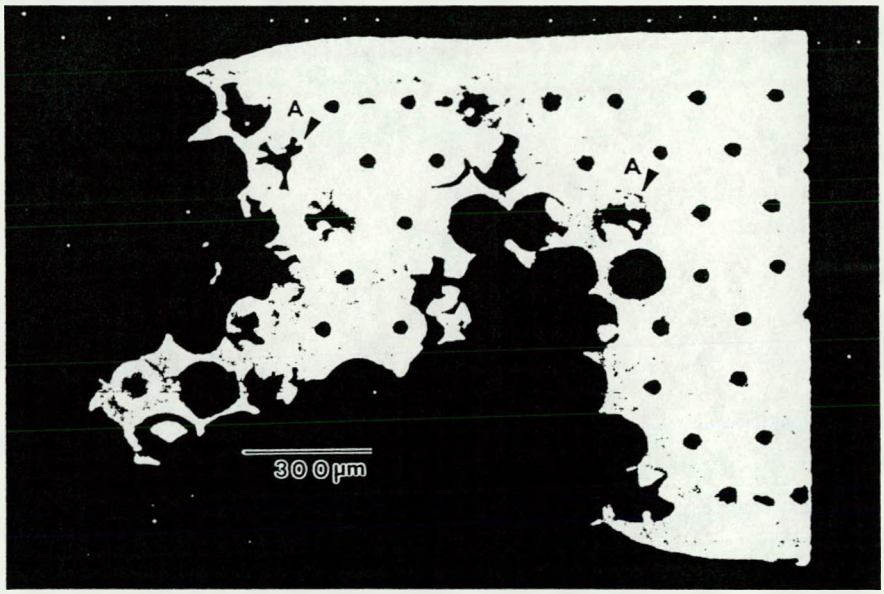

Figure 4: XTM image beneath the fracture surface in a SiC fiber / Al matrix composite failed in tension. Significant plastic deformation of the matrix is observed, as is the fracture behavior of the fibers (arrows marked A). Examination of the fiber fractures indicate that failure occured at the graphite core and not at the SiC/Al interphase.

The second example is a 1.5 mm CAS (calcium aluminum silicate) matrix—SCS6 fiber composite[21]. The fibers are arranged in a 0/90 cross-ply stacking sequence. Absorption data were acquired at 0.5 degree angular increments using an x-ray energy of 20 keV. The pixel sampling size was 5.6-μm, and 250 contiguous slices were imaged. Figure 5a is an XTM micrograph taken 0.9 mm beneath the surface of the composite panel at 50X magnification. Figure 5b is the corresponding SEM micrograph showing the same location. The SEM photomicrograph was obtained subsequent to the XTM examination by sectioning.

It is of interest to compare the two observations. The XTM image shows a crack running from left to right across the specimen approximately 12 μm (.0005") above a 90° fiber. This same crack is also observed in the optical micrograph. SEM examination of this crack reveals it to be less than 1.5 μm (.00004") across along its entire length. Even though the pixel sampling size is 5.6 μm, the high contrast provided by the crack makes it possible to image features much smaller. This is an important point: spatial resolution and feature detectability are not the same, and pixel size as a measure of system performance is a meaningless concept unless it is related to the overall resolution of all of the individual components in the system.

In addition to the crack, a small piece of broken fiber can be seen in both the XTM and the optical images. This broken fiber fragment lies between the second and third fiber plies from the top of the image. Broken pieces of fiber may act as stress concentrators for initiating cracks, and therefore, it is important to be able to detect these low contrast flaws.

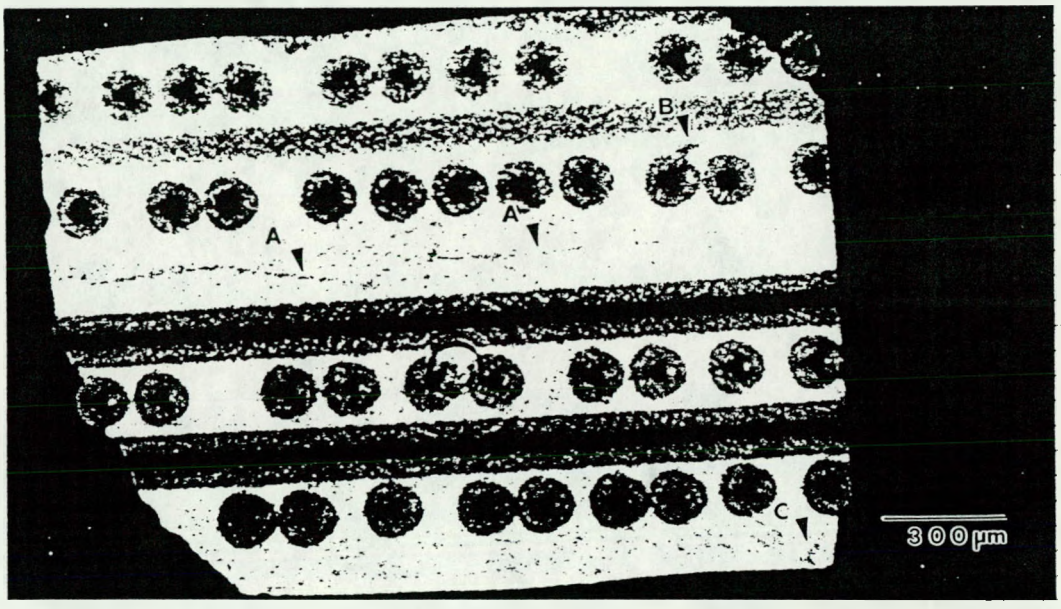

Figure 5a: XTM micrograph of a CAS matrix/SCS6 fiber 0/90 composite. Arrows marked A highlight a microcrack running across the width of the sample. This crack is 1.5 μm at its widest extent. Arrow marked B shows a broken fiber fragment lodged between fiber plies. Arrow marked C shows another microcrack in the composite.

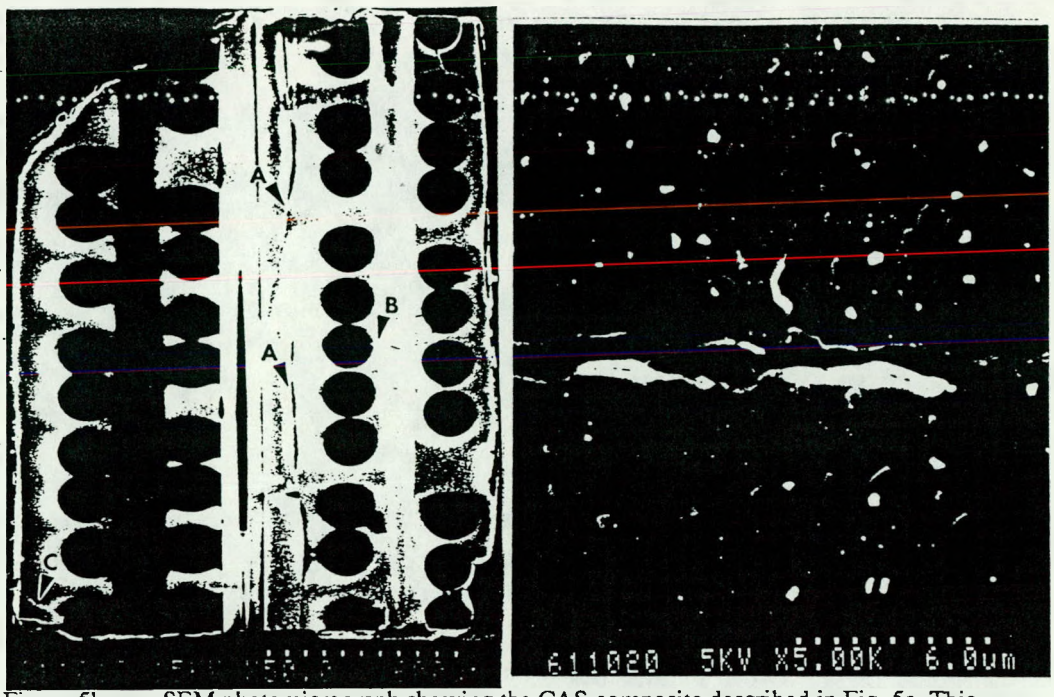

Figure 5b: SEM photomicrograph showing the CAS composite described in Fig. 5a. This SEM micrograph was obtained after sectioning the sample to the same slice plane as the XTM image. The SEM shows the same crack (marked with arrow A) as displayed in the XTM image. In addition, the SEM image shows the crack continuing across a fiber ply (arrow B). This crack extension was not seen in the XTM image, and therefore we believe it to be a result of stress relief upon polishing. On the right side of 5b is a high magnification image (5000X) of the crack imaged by the XTM, indicating that it is less than 1.5μm.

The final example is a SiC matrix—Nicalon fiber (amorphous SiC) composite. The Nicalon fibers vary in diameter from 10–20 μm. The fibers are organized into bundles called tows (containing approximately 500 fibers), and these tows are in turn woven into a cross–ply cloth. The fiber cloth is formed into a near net shape component, and then a SiC matrix is grown around the fibers by infiltrating a reactive gas mixture at high temperature[22]. Several types of porosity can be left behind from the chemical vapor infiltration (CVI) process. The porosity is generally broken down, however, into two types: microporosity, consisting of pores within a tow, and macroporosity, consisting of any type of porosity lying outside of the tow. The type, size and interconnectedness of the porosity directly influence the permeability of the chemical vapor into the composite. The pores may also act as nucleation sites for cracks. Because of the geometric complexity of this type of composite, a three–dimensional imaging technique has a great advantage over two–dimensional techniques in studying the origin of pores, their interconnectedness, and their subsequent influence on mechanical properties.

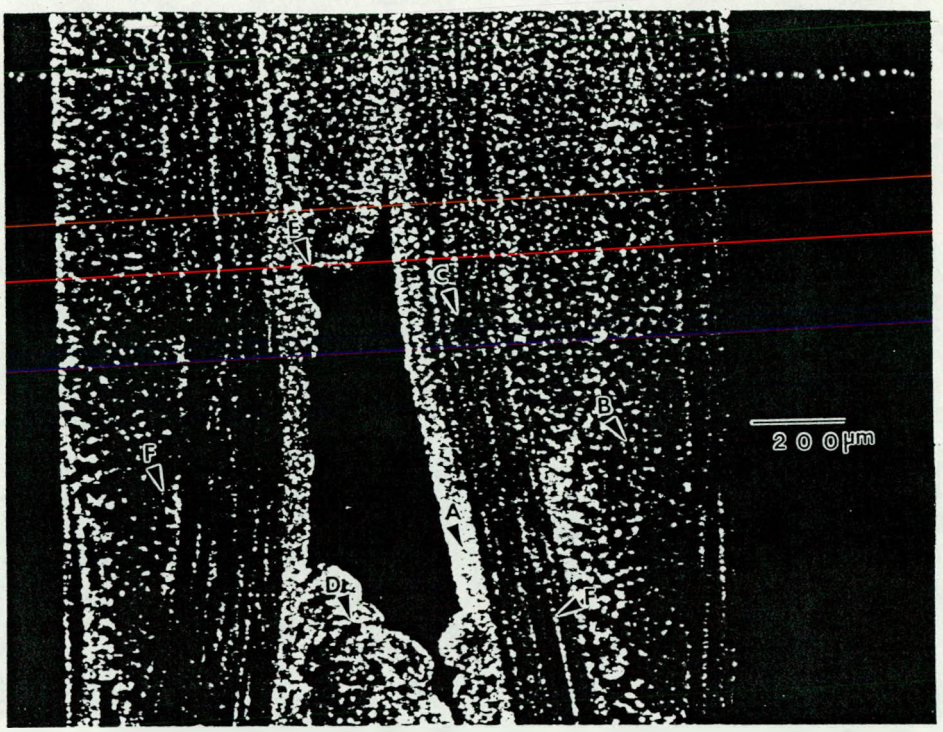

Figure 7: XTM image of a Nicalon fiber/SiC woven composite. The fully–dense SiC is marked with arrow A. A fiber tow oriented perpendicular to the cross section is marked with arrow B. A fiber tow oriented in the plane of the cross section is marked with arrow C. Individual fibers (arrow D) can be seen in the tow peripheries. Also resolved are macropores (arrow E) and micropores (arrow F).

Figure 7 is an XTM image of a fully reacted SiC–Nicalon woven composite. This preliminary study was designed to determine whether or not XTM can image micro– and macroporosity, and also whether the present contrast sensitivity and spatial resolution of the technique is adequate for imaging the fiber tows in the SiC matrix. The XTM image in Fig. 7 clearly distinguishes between the Nicalon and SiC, and shows both types of porosity. Near the peripheries of the tow, it is possible to identify individual fibers (10–20 μm). The magnification will need to be increased to resolve individual fibers in the tow interiors.

Future Directions

It is highly unlikely that XTM will ever achieve the spatial resolution of SEM. XTM's principal advantage, an extremely important advantage, lies in its noninvasive, three-dimensional capability. Coupling XTM to other, more destructive techniques, will greatly expand our understanding of the time-evolution of materials microstructures. In order for XTM to realize this potential, however, in-situ inspection capabilities must be developed. These capabilities will include tensile load cells and high temperature stages.

We have recently tested a prototype load frame which allows XTM studies to be performed on samples while they are under tensile load[23]. In its prototype configuration, the load frame rests upon a single rotational stage—the load from the grips being suppoted by a semi–transparent x-ray window. Though the x-ray window alters the DC value of the XTM images due to incomplete normalization of the reference beam, we have demonstrated an ability to open up and image cracks using this cell up to 42ksi tensile load. It is important to note that vibration and drift in the sample position must be kept below a micrometer during the XTM measurements.

Figure 8 shows the load frame configured for use with a conventional x-ray generator. At the right in Figure 8 are shown longitudinal and transverse XTM sections through the notched region of an Al–Li alloy under 42ksi tensile load. The opened crack is easily visualized, whereas at 0 ksi load the crack is nearly invisible. The noise in the image is due to un–normalized absorption in the x-ray window. A second generation load cell is now being designed which will eliminate the x–ray window.

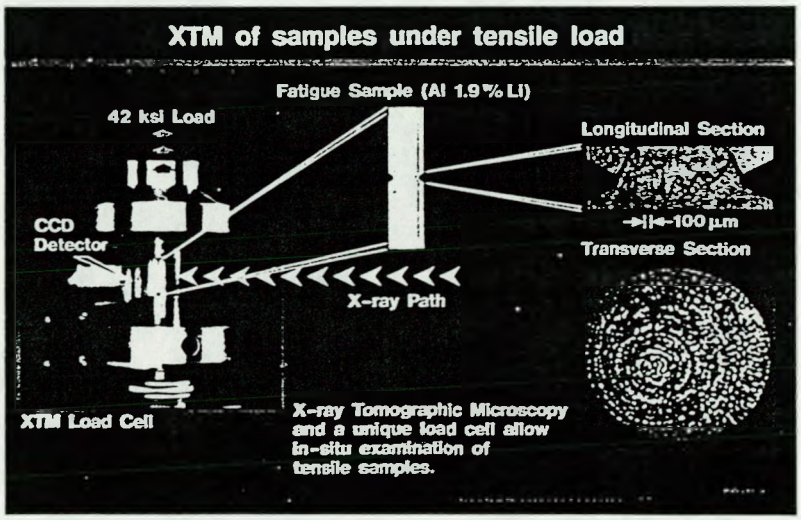

Figure 8: *In–situ* load frame for perfoming XTM on samples under tensile load.

In addition to *in–situ* load frames, it will be necessary to image larger samples with at least the same spatial resolution, if not better, as that which we have already demonstrated. In the present XTM design, and in all commercially available systems, the sample is constrained to always remain within the field of view of the detector during rotation. The CCD detector used for these examples has approximately 1000 pixels (detector elements) across the field of view. This allows us to image a 1 cm wide sample with an equivalent 10 μm pixel. With a recently acquired 2k x 2k element CCD array, the same sample can be imaged using 5 μm pixels. An obvious approach is to obtain larger format CCDs as they become available. This approach is impractical, however, because the cost of these CCDs is high, and the availability is low. In addition, the data storage requirements become enormous with increasing format.

Two other options exist for increasing the sample size with the present XTM design. The first is to use translate–rotate geometries. In this manner, the sample is translated across the field of view. This method requires multiple exposures and an extremely tight tolerance on pixel registration. Though greatly increasing the acquisition time, the translate–rotate method will allow imaging larger samples with small format CCDs. However, data storage requirements will remain large using this method.

An alternative approach, and the one which we are pursuing, is the region of interest (ROI) method. Using the ROI method, the entire sample is no longer constrained to remain within the field of view; rather, only a region of interest needs to remain within view during rotation. We have been making progress with the ROI method, and success with the method has now been obtained with artificial data. Application of the ROI method to actual experimental data is now being undertaken.

CONCLUSIONS

We have described an x–ray tomographic microscope which has sufficient resolution and contrast sensitivity to provide valuable microstructural information on engineering materials. The microscope can operate using both conventional and synchrotron sources of radiation. The approach to x–ray microscopy outlined in this paper differs from other efforts in that we are developing the technique to image small features in large samples at high x–ray energy.

X–ray tomographic microscopy is beginning to be applied to materials science studies of composite materials. Efforts are underway to use XTM in studies of fatigue and failure in metal matrix composites and also to study chemical vapor infiltration of ceramic composites. Furthermore, a recently developed tensile loading frame has been used in initial studies of crack closure in high strength Al alloys[23].

The application of XTM to materials studies has only just begun. The use of XTM with other imaging modalities, for example ultrasound, MRI, and electron microscopy, promises to greatly improve our understanding of processing and failure in advanced materials.

ACKNOWLEDGEMENTS

This work was performed under the auspices of the U.S. Department of Energy by Lawrence Livermore National Laboratory under contract No. W-7405-Eng-48 and by Sandia National Laboratories, Livermore under contract AT-29-1-789. Some of this work was also supported by the BMFT (Bonn, Germany) under contract 03-BO1DOR. The authors acknowledge the support of the Advanced Industrial Materials Program, Office of Industrial Technologies, U.S. Department of Energy. The XTM experiments were performed at the Cornell High Energy Synchrotron Source (CHESS), which is supported by NSF grants to B.W. Batterman. The authors would like to show their appreciation for the help provided by D.H. Bilderback and his staff at CHESS. We would also like to thank the contributions of W. Massey (LLNL) for his support in all phases of the work, as well as thank J.Celeste (LLNL) and D. Weirup (LLNL) for their help in conducting the experiments. Load frame development supported in part by Office of Naval Research under grant N0014-89J-1708.

REFERENCES

1. J.H. Kinney, et al., **J. Mat. Res., 5,** 1123 (1990).
2. U.Bonse, et al., accepted for publication in J. Mat. Science, (1990).
3. G.T. Herman, *Image Reconstruction from Projections: The Fundamentals of Computerized Tomography* (Academic Press, New York, 1980).
4. J.C. Elliott and S.D. Dover, **J. Microscopy 126,** 211 (1982).
5. S.R. Stock, A. Guvenilir, J.C. Elliott, P. Anderson, S.D. Dover and D.K. Bowen, in *Advanced Characterization Techniques for Ceramics* (American Ceramic Society, Westervill, Ohio, in press).
6. F.H. Seguin, P.Burstein, P.J. Bjorkholm, F. Homburger, and R.A. Adams, **Appl. Opt. 24,** 4117 (1985).
7. M.K. Cueman, L.J. Thomas, C. Trzaskos, and C. Greskovich, in *Review of Progress in Quantitative Nondestructive Evaluation,* D.O. Thompson and Dale E. Chimenti, eds. (Plenum Press, New York, 1989), Vol. 8A. p. 431.
8. U.Bonse, Q.Johnson, M.Nichols, R. Nusshardt, S. Krasnicki and J. Kinney, **Nucl. Instrum. Methods A246,** 644 (1986).
9. L. A. Feldkamp, G. Jesion, and D.J. Kubinski,in *Review of Progress in Quantitative Nondestructive Evaluation,* D.O. Thompson and Dale E. Chimenti, eds. (Plenum Press, New York, 1989), Vol. 8A., 381.
10. L.A. Feldkamp, L.C. Davis, and J.W. Kress, **J. Opt. Soc. A1,** 612 (1984).
11. H.E. Martz, S.G. Azevedo, J.M. Brase, K.E. Waltjen and D.J. Schneberk, **Int. Jour. of Radiation Applications and Instrumentation Part A** (UCRL - 98492 Livermore Report) to be published 1990.
12. J. Kinney, Q.Johnson, U.Bonse, R. Nusshardt,andM.C. Nichols, **SPIE 691,** 43 (1986).
13. J.H. Kinney, Q.C. Johnson, R.A. Saroyan, M.C. Nichols, U.Bonse, R. Nusshardt and R. Pahl, **Rev. Sci. Instrum. 59,** 196 (1988).
14. M.C. Nichols, et al. , **Rev. Sci. Instrum. 60,** 2475 (1989).
15. U.Bonse, et al., **Rev. Sci. Instrum. 60,** 2478 (1989).
16. B.P. Flannery, H.Deckman, W. Roberge, and K. D'Amico, **Science 237,** 1439 (1987).
17. H.W. Deckman, K.L. D'Amico, J.H. Dunsuir, B.P. Flannery and S.M. Gruner, in *Advances in X-ray Analysis* 32, 641 (Plenum Press, New York 1989).
18. M. Ito, M. Yamaguchi, K. Oba, and S.-Kanzo,**IEEE Transactions on Nuclear Science NS-34,** 401 (1987).
19. T.P. Wilcox, Jr. and E. M. Lent, in *COG- A Particle Transport Code Designed to Solve the Boltzmann Equation for Deep-Penetration Problems,* **M-221-1** (Lawrence Livermore National Laboratory, Livermore California 1989).
20. T.M. Breunig, S.R. Stock, J.H. Kinney, A. Guvenilir, and M.C. Nichols, presented at the MRS Fall Meeting, Boston, November 1990 (to be published in these proceedings).
21. Sample provided by D. Copley, GE Aircraft Engines, Cincinnati,OH.
22. T.L. Starr, Ceramic Engineering and Science Proceedings, 8, 951 (1987).
23. T.M. Breunig, S.R. Stock, S.D. Antolovich, J.Kinney,W. Massey and M.C. Nichols, Proceedings of the 22nd National Symposium on Fracture Mechanics, June 1990, Atlanta GA (to be published in a STP by ASTM).